# Cortical hypoperfusion and reduced cerebral metabolic rate of oxygen in the arcA mouse model of Alzheimer's disease

Ni, Ruiqing ; Rudin, Markus ; Klohs, Jan

Abstract: The effect of cerebral amyloidosis on cerebral hemodynamics was investigated with photoacoustic tomography (PAT) and magnetic resonance imaging (MRI). First, the sensitivity and robustness of PAT for deriving metrics of vascular and tissue oxygenation in the murine brain was assessed in wild-type mice with a hyperoxia-normoxia challenge. Secondly, cerebral oxygenation was assessed in young and aged arcA mice and wild-type controls with PAT, while cerebral blood flow (CBF) was determined by perfusion MRI. The investigations revealed that PAT can sensitively and robustly detect physiological changes in vascular and tissue oxygenation. An advanced stage of cerebral amyloidosis in arcA mice is accompanied by a decreases in cortical CBF and the cerebral metabolic rate of oxygen (CMRO), as oxygen extraction fraction (OEF) has been found unaffected. Thus, PAT constitutes a robust non-invasive tool for deriving metrics of tissue oxygenation, extraction and metabolism in the mouse brain under physiological and disease states.

DOI: https://doi.org/10.1016/j.pacs.2018.04.001

Photoacoustics 10 (2018) 38–47

Contents lists available at ScienceDirect

Photoacoustics

journal homepage: www.elsevier.com/locate/pacs

Research article

# Cortical hypoperfusion and reduced cerebral metabolic rate of oxygen in the arcAβ mouse model of Alzheimer's disease

Ruiqing Ni[a], Markus Rudin[a,b], Jan Klohs[a,*]

[a] Institute for Biomedical Engineering, University of Zurich & ETH Zurich, 8093 Zurich, Switzerland
[b] Institute of Pharmacology and Toxicology, University of Zurich, 8008 Zurich, Switzerland

ARTICLE INFO

*Article history:*
Received 14 November 2017
Received in revised form 14 February 2018
Accepted 3 April 2018
Available online 12 April 2018

*Keywords:*
Alzheimer's disease
Cerebral amyloidosis
Cerebral blood flow
Cerebral metabolic rate of oxygen
Photoacoustic tomography
Mouse model
Oxygen extraction fraction

ABSTRACT

The effect of cerebral amyloidosis on cerebral hemodynamics was investigated with photoacoustic tomography (PAT) and magnetic resonance imaging (MRI). First, the sensitivity and robustness of PAT for deriving metrics of vascular and tissue oxygenation in the murine brain was assessed in wild-type mice with a hyperoxia-normoxia challenge. Secondly, cerebral oxygenation was assessed in young and aged arcAβ mice and wild-type controls with PAT, while cerebral blood flow (CBF) was determined by perfusion MRI. The investigations revealed that PAT can sensitively and robustly detect physiological changes in vascular and tissue oxygenation. An advanced stage of cerebral amyloidosis in arcAβ mice is accompanied by a decreases in cortical CBF and the cerebral metabolic rate of oxygen ($CMRO_2$), as oxygen extraction fraction (OEF) has been found unaffected. Thus, PAT constitutes a robust non-invasive tool for deriving metrics of tissue oxygenation, extraction and metabolism in the mouse brain under physiological and disease states.


## 1. Introduction

The brain has a very high demand for oxygen compared to other organs (it utilizes approximately 20% of the body's total oxygen consumption), making tight regulation of cerebral blood flow (CBF) and oxygen delivery critical for brain function [1]. The regional quantification of oxygen saturation ($SO_2$), brain oxygen extraction fraction (OEF) and, in conjunction with perfusion imaging for CBF, the cerebral metabolic rate of oxygen ($CMRO_2$) are key measures of brain hemodynamic function. Quantification of these parameters has helped to elucidate brain functional physiology and holds translational potential as a clinical tool for evaluating neurological disorders such as stroke, brain tumors and Alzheimer's disease (AD) and other age-related pathologies.

AD is associated with vascular dysfunction which partakes in the pathogenesis of the disease [2]. Patients with AD show regional hypoperfusion, decreased levels of oxygenated hemoglobin ($HbO_2$) and tissue oxygenation [3], as well as capillary dysfunction at an early disease stage, reported to be associated with cognitive symptom severity and neurodegeneration [4]. $^{15}O$ PET study in AD patients showed reduced $CMRO_2$ compare to healthy controls [5]. Transgenic mice overexpressing human amyloid precursor protein (APP) are widely used models of AD. These mice display progressive amyloidosis in the brain and enable studying the influence of amyloid-beta (Aβ) accumulation on vascular function [6]. In APP mice hypoperfusion and capillary dysfunction [7] have been described, but the relationships to oxygen transport and metabolism have not yet been investigated. Moreover, methods which are non-invasive possess a high sensitivity and spatial resolution, cover a large field-of-view and are easy to apply are highly desired.

In recent years, a variety of biological and medical imaging techniques have been developed to assess cerebral oxygenation in animal models and in humans. Positron emission tomography (PET) with $^{15}O$ is considered the gold standard for the whole-brain oxygenation measurement in clinical setting [8]. While the method has been applied to mice [9], the method suffers from low spatial resolution which limits its usefulness for studying small species Moreover, the short half-life of [$^{15}O$] requires an on-site cyclotron, which restricts the widespread use of this approach. Alternatively, MRI-based techniques such as blood oxygenation level-dependent (BOLD), quantitative BOLD, susceptometry, $T_2$-relaxation-under-spin-tagging and $^{17}O$ MR spectroscopy among others have been proposed for mapping oxygenation [10]. Measurements of BOLD and CBF in conjunction with hypercapnic or hyperoxic respiratory challenges have been proposed for measuring relative changes and absolute value of $CMRO_2$ [11]. However MR methods that infer the regional concentration of oxygen by measuring tissue $R_2$, $R_2$' or $R_2$* relaxation rates (such as BOLD) or bulk susceptibility, which is

* Corresponding author at: Institute for Biomedical Engineering, University of Zurich and ETH Zurich, Valdimir-Prelog-Weg 4, 8093 Zurich, Switzerland.
*E-mail address:* klohs@biomed.ee.ethz.ch (J. Klohs).

https://doi.org/10.1016/j.pacs.2018.04.001

sensitive to paramagnetic compounds such as Hb, are prone to confounder as non-vascular tissue compartments invariably contribute to the signals or are sensitive to changes in vessel caliber and orientation. This limits their applicability for characterizing brain diseases that involve significant remodeling of the vasculature such as in arcAβ mouse model [12–14].

Optical imaging such as Doppler optical coherence tomography [15], laser Doppler spectroscopy [16], two-photon [17], near-infrared spectroscopy [18], photoacoustic microscopy [19,20], and single-impulse panoramic photoacoustic computed tomography [21] have been used for deriving metrics of regional tissue oxygenation in small animals; yet these techniques, are often invasive, or suffer from a small field-of-view and limited depth penetration. By using multiple wavelengths for illuminating and spectral unmixing algorithms, photoacoustic tomography (PAT) resolves signal contribution from different photoabsorbing molecules in tissue simultaneously based on their spectral properties [22]. In biological tissue major absorbers such as hemoglobin serves as an endogenous contrast agent for PAT [23,24]. As hemoglobins display significant absorption values in the red and near-infrared spectral domain, PAT allows the non-invasive assessment of hemodynamic parameters relatively deep in tissue (mm range) [25] in the brains of rats and mice [26].

Here we describe an approach to estimate OEF and $CMRO_2$ in mouse brain based on PAT estimates of arterial oxygen saturation ($S_aO_2$) in the middle cerebral artery (MCA) and venous oxygen saturation ($S_vO_2$) in the superior sagittal sinus (SSS) as well as in cortical tissue oxygenation ($S_tO_2$) of mouse in combination with CBF measurements by using perfusion magnetic resonance imaging (MRI). We found reduced cortical CBF in aged transgenic arcAβ mice, which displays abundant parenchymal and vascular amyloid deposition [24,27]. Due to the inability of the vascular system to compensate the decrease in oxygen delivery by increasing the OEF, $CMRO_2$ values were found to be significantly decreased.

## 2. Methods

### 2.1. Animal model

Ten female non-transgenic C57BL/6 mice (12 weeks) were purchased from Janvier (France) and used in the oxygen-challenge PAT validation experiment for deriving $S_aO_2$ in the MCA, $S_vO_2$ in the SSS and $S_tO_2$ in the cortical tissue. Eighteen transgenic arcAβ mice overexpressing the human APP695 transgene containing the Swedish (K670N/M671L) and arctic (E693G) mutation under the control of the prion protein promoter and eighteen age-matched non-transgenic C57BL/6 littermates of both sexes were bred at Phenomic Center ETH Zurich (Switzerland) and were assessed at 6- and 24-months of age. ArcAβ mice are characterized by Aβ plaque formation at 6-months of age together with a pronounced cerebral amyloid angiopathy [27]. Animals were housed in ventilated cages inside a temperature-controlled room, under a 12-h dark/light cycle. Pelleted food (3437PXL15, CARGILL) and water were provided *ad-libitum*. Using StatMate (Graphpad prism 7.0, USA) a sample size of $n = 6$ per group was calculated a priory for the primary end point CBF, a fixed effect omnibus, one-way ANOVA with four groups, and an effect size $f = 0.78$, $\alpha = 0.05$ and $\beta = 0.2$. Consequently, group sizes $n > 6$ were used.

### 2.2. Perfusion MRI protocol

MRI was performed on a 7/16 small animal MR Pharmascan (Bruker Biospin GmbH, Ettlingen, Germany) equipped with an actively shielded gradient set of 760 mT/m with a 80 μs rise time and operated by a Paravision 6.0 software platform (Bruker Biospin GmbH, Germany). We used a circular polarized volume resonator for signal transmission and an actively decoupled mouse brain quadrature surface coil with integrated combiner and preamplifier for signal receiving (Bruker BioSpin, Germany). Thirty-three mice were anesthetized with an initial dose of 4% isoflurane (Abbott, Cham, Switzerland) in oxygen/air (200:800 mL/min) mixture in the induction box and were maintained at 1.5% isoflurane in oxygen/air (100:400 mL/min) mixture supplied via a nose cone. Mice were placed in prone position on a water-heated support to keep body temperature at 36.5 ± 0.5 °C monitored with a rectal temperature probe. $T_2$-weighted anatomical reference images were acquired in coronal and sagittal orientations and served for accurate positioning of the arterial spin labeling (ASL) slice (Fig. 3A). A spin-echo sequence was used with rapid acquisition relaxation enhancement, echo time = 33 ms; relaxation time = 2500 ms; rapid acquisition relaxation enhancement factor = 8; flip angle = 90°; fifteen sagittal slices of 1 mm thickness; field-of-view = 20 × 20 mm; image matrix = 256 × 256; spatial resolution = 78 × 78 μm; resulting in an acquisition time of 2 min 40 s.

Perfusion was measured under resting conditions using an ASL method with a flow sensitive alternating inversion recovery technique. Fieldmap-based shimming was performed using the automated MAPshim routine to improve the homogeneity of the magnetic field. A spin-echo planar imaging sequence preceded by a 180° hyperbolic secant RF inversion pulse was used with echo time = 12.47 ms; relaxation time = 12000 ms; flip angle = 90°. One axial slide of 1 mm thickness was acquired approximately at Bregma −1.46 mm with a field-of-view = 20 × 20 mm; image matrix = 128 × 96, with a spatial resolution = 156 μm × 208 μm. Inversion parameters were: inversion slab thickness = 4 mm, slice margin = 1.5 mm. Sixteen images with increasing inversion times (10 s, 50–3000 ms) were obtained for $T_1$ calculations, with a total scan time of 11 min and 55 s. Inversion recovery data from the imaging slices was acquired after selective inversion interleaved with non-selective inversion. For each mouse brain in the current study, a $T_2$-weighted anatomical image was acquired at the same position as the ASL slice for drawing regions of interest (ROI). Paxinos mouse brain atlas was used as the anatomical reference for scan and analysis.

### 2.3. PAT and image paradigm

For PAT the inVision 128 small animal multi-spectral optoacoustic tomography system (iThera Medical GmbH, Munich, Germany) was used as described before [28]. We first tested the sensitivity and repeatability of PAT for detecting physiological changes in blood and tissue oxygenation by applying an oxygen challenge. Longitudinal PAT measurements were performed in 10 wild-type mice for 15 min. Mice were anesthetized with an oxygen/air mixture (200:800 mL/min) in the induction box and anesthesia was maintained at 1.5% isoflurane supplied via a nose cone under normal air supply (oxygen/air 100:400 mL/min). The hyperoxia challenge consists of two cycles: normoxia (oxygen/air 0:500 mL/min, fraction of inspired oxygen $FiO_2 = 20\%$, 3 min) – 100% hyperoxia (oxygen/air 500:0 mL/min, $FiO_2 = 100\%$, 3 min) during continuous imaging were performed based on previous photoacoustic microscopy setting [21] as illustrated in Fig. 1 and Supplementary Fig. 1. The paradigm allowed us to compare the repeatability of the approach (comparing test and retest values). The body temperature of the mouse was kept at 36.5 °C while imaging by adjusting the temperature of the water chamber. Laser excitation pulses of 9 ns were delivered at five wavelengths (715, 730, 760, 800, 850 nm); one coronal slice was examined, 1 average was collected [28]. Data were acquired continuously for 15 min resulting in 360 frames for each mouse corresponding to an acquisition time of 2.5 s per image frame.

In the second part of the study we assessed the capability of PAT to detect alteration in oxygen saturation, extraction and

metabolism due to amyloid pathology. Metrics of vascular and tissue oxygenation were derived from multi-spectral PAT measurements of arcAβ ($n = 17$) and wild-type ($n = 16$) mice of 6-months and 24-months of age. Mice were anesthetized with an oxygen/air mixture (200:800 mL/min) in the induction box and anesthesia maintained with 1.5% isoflurane in oxygen/air (100:400 mL/min) via a nose cone. Imaging was performed at five wavelengths 715, 730, 760, 800, 850 nm on coronal slices, with 10 averages per slice. Rostral caudal brain coverage extended over a length of approximately 12 mm with a step size of 0.3 mm resulting 40 slices. Data acquisition time was 4 min.

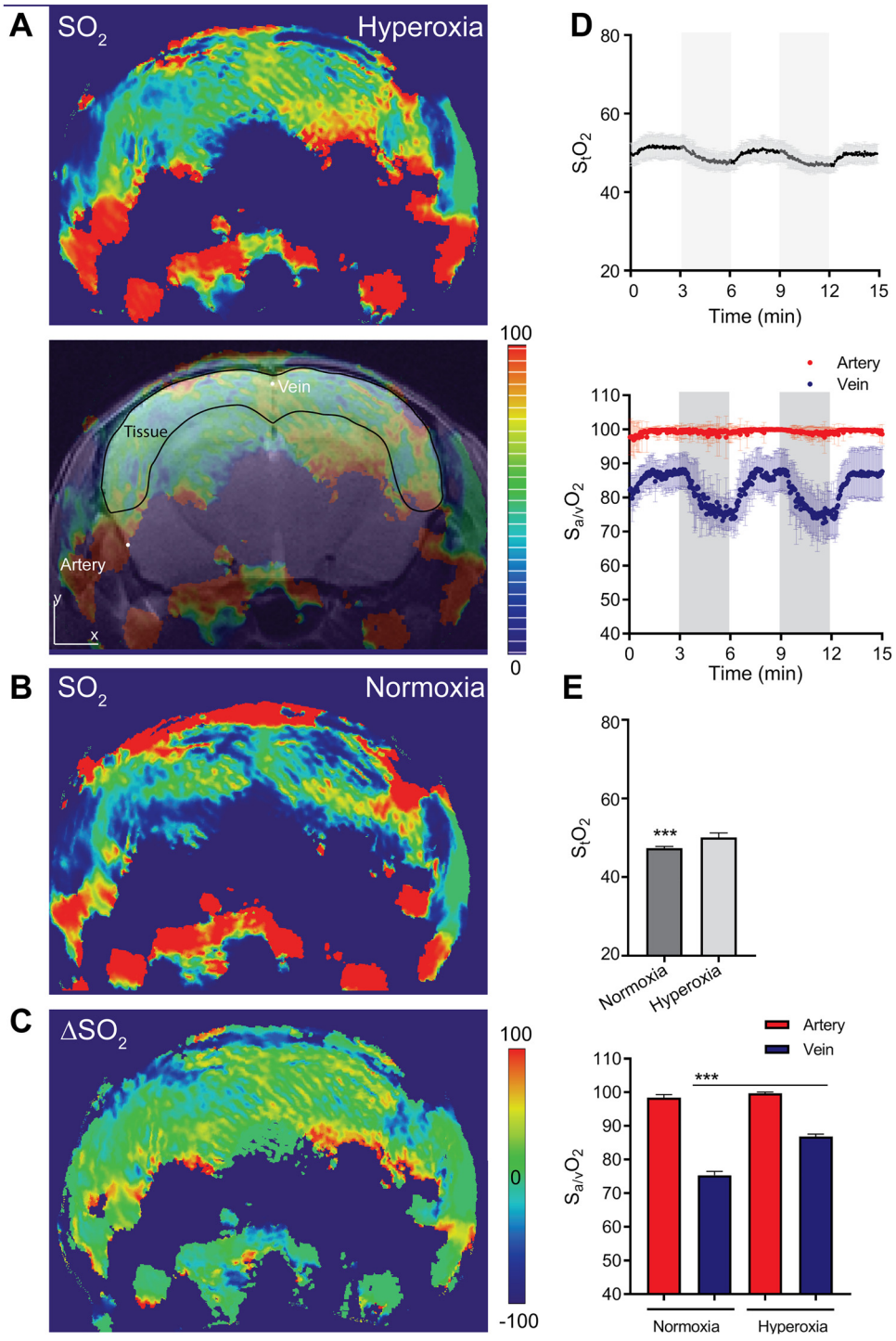


**Fig. 1.** *In vivo* brain oxygen saturation in wild-type mice under oxygen challenge with photoacoustic tomography. Representative coronal $SO_2$ map derived from PAT measurements of Hb and $HbO_2$ of a head of a wild-type mouse under (A) hyperoxic and (B) normoxic conditions, approximatly Bregma $-1.5 \pm 0.3$ mm; overlaid with $T_2$-weighted magnetic resonance image (C) $\Delta SO_2$ map to show differences in oxygenation in hyperoxia-normoxia challenge; (D) Cortical $S_tO_2$ and $S_vO_2$ derived from PAT measurements during normoxia (grey region) and hyperoxia in brain of wild-type mice ($n = 10$); (E) Significant differences between cortical $S_tO_2$ and $S_vO_2$ under normoxia and hyperoxia condition. Mann-Whitney Rank Sum Test, *** $p < 0.001$; $S_tO_2$: tissue oxygen saturation; $S_aO_2$: arterial oxygen saturation $S_vO_2$: venous oxygen saturation.

### 2.4. Perfusion MRI data analysis

ROIs were drawn over the cerebral cortex and thalamus on axial $T_2$-weighted anatomical scans and then transferred to the CBF maps using AFNI (NIH, USA, Fig. 3A). For CBF calculation, the flow sensitive alternating inversion recovery images with different $T_{1selective}$ were realigned and resliced over the first $T_1$ using a rigid-body model. Determination of $T_{1selective}$ and $T_{1global}$ were performed by fitting the averaged signal intensities in each ROIs with 3-parameters mono-exponential $T_1$ relaxation curve. CBF in ROIs was calculated from both $T_1$ values using the Eq. (1) in MATLAB R2015b (Mathworks, MA, USA):

$$CBF/\lambda = \frac{T_{1global}}{T_{1blood}}\left(\frac{1}{T_{1selective}} - \frac{1}{T_{1global}}\right) \quad (1)$$

where CBF is the amount of blood passing through the brain tissue in mL/100 g/min, $\lambda$ is the blood/tissue partition coefficient for water, assumed to be 0.9 mL/g [29] and $T_{1blood}$ was assumed to be 2.007 s at 7 T [30].

### 2.5. PAT data post-processing and analysis

PAT images were reconstructed using a model linear algorithm with a non-negativity constraint imposed during inversion. Linear unmixing was applied to resolve signals from Hb/$HbO_2$. Six C57BL/6 mice with prominent dark pigment on their skin over the head which interferes with PAT measurements were excluded from data analysis. PAT images were co-registered and overlaid with $T_2$-weighted MRI scans using a landmark-based registration with Matlab (R2015a, Mathworks, USA) (https://codeocean.com/

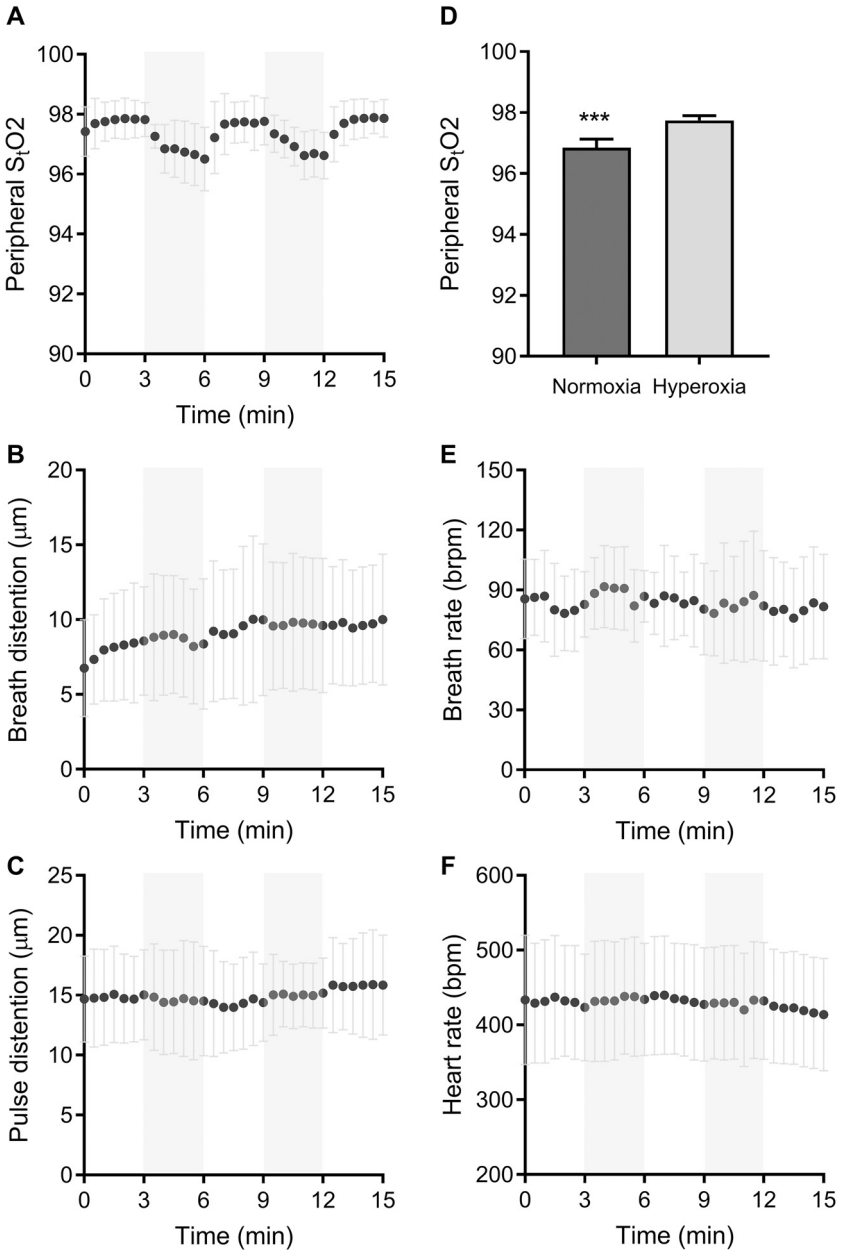


**Fig. 2.** Physiological parameters estimated by oximetry during oxygen challenge. (A-E) Time course of peripheral oxygen saturation (%), breath distention (μm), pulse distention (μm), heart rate (beat per min, bpm), respiratory rate (breath rate per min, brpm) measured under normoxia (grey region, 3–6 and 9–12 min) and hyperoxia (0–3, 6–9 and 12–15 min) in wild-type mice ($n = 10$); F) Significant difference between peripheral oxygen saturation% under normoxia and hyperoxia. Mann-Whitney Rank Sum Test, $^{***}p < 0.0001$;.

algorithm/910653cc-f008-4573-9b8c-92dde419528c/code) as described previously [31]. Firstly, the anatomical PAT image was aligned with the $T_2$-weighted MR image and 6–7 pairs of anatomical landmarks were manually selected. Secondly, non-reflective similarity transformation was applied to PAT images after processing MR images calculated based on the least square algorithm of the landmark pairs in both PAT and MR images. Rotation, scaling and transformation were applied during registration. As PAT images of Hb, $HbO_2$ share the same coordinates with the intrinsic anatomical images, the same co-registration transformation was applied to the Hb, $HbO_2$ and the computed $SO_2$ images. The resulting images were overlaid on the $T_2$-MRI images in multiple channels. ROIs were drawn over the axial overlaid PAT/MR images using ImageJ (NIH, U.S.A.). As the vessels have a diameter of 140 μm, on coronal cross-sections of the mouse head, circular ROIs of diameter 140 μm, area 0.0049 $mm^2$ were delineated at MCA for calculating $S_aO_2$; and at SSS for calculating $S_vO_2$ on the computed $SO_2$ image. ROIs with an area of approx. 24 $mm^2$ were delineated over the cortex for quantifying tissue $S_tO_2$ (illustrated in Fig. 1A). Values for oxygen saturation in tissue and large vessel ($S_iO_2$ or $S_{a/v}O_2$) was calculated according to:

$$S_iO_2 = HbO_{2,i}/(Hb_i + HbO_{2i}) \times 100 \quad (2)$$

With $i = t,a,v$. PAT will resolve absolute values of $S_iO_2$ if the recorded signal is directly related to the absorbed optical energy distribution, with knowledge of the light fluence distribution, system response and Grüneisen parameter [32,33]. Thus the values derived in this study represent metrics of the PAT measurements rather than absolute $SO_2$ values.

The OEF values were obtained as:

$$OEF = (S_aO_2 - S_vO_2)/S_aO_2 \quad (3)$$

and hyperoxia induced change in tissue oxygenation as:

$$\Delta S_iO_2 = \overline{\text{hyperoxia } S_iO_2} - \overline{hypoxia\ S_iO_2} \quad (4)$$

With $S_iO_2$ defined in Eq. (2). As $S_iO_2$ values became stable within two min after switching the oxygen concentration of the gas supply (Fig. 2), the values measured during the final min of each three-min interval were used for calculating the mean ($\overline{hyperoxia\ S_iO_2}$) or ($\overline{hyperoxia\ S_iO_2}$) and differences in oxygen saturation ($\Delta SO_2$). Maps of $SO_2$, $\Delta SO_2$, $\Delta Hb$ and $\Delta HbO_2$ for hyperoxia challenge were calculated using ImageJ (NIH, U.S.A.). The $SO_2$ images computed directly from $HbO_2$/Hb image were used for validation of $SO_2$ values derived from ROI analysis of the Hb and $HbO_2$ map. Based on the Fick's principle, $CMRO_2$ can be derived from the arteriovenous oxygen gradient:

$$CMRO_2 = CBF \times (S_aO_2 - S_vO_2) \times C_a \quad (5)$$

*Where* $C_a$ is a constant representing the maximal amount of oxygen carrying capacity of a unit volume of blood at a hematocrit of 0.44, assumed to be 833.7 μmol $O_2$/100 mL blood [34].

### 2.6. Physiological monitoring

The physiological conditions of ten wild-type mice in oxygen challenged PAT measurement were monitored using MouseOx Plus oximeter (Starr Life Science, U.S.A.). Breathe distention, pulse distention, heart rate, percentage of peripheral oxygen saturation and breath rate were recorded every 30 s over 15 min with the same oxygen challenge and anesthesia paradigm using an infrared sensor which was placed on the shaved upper hind limb of the wild-type mice ($n = 10$).

### 2.7. Statistics

All data are present as mean ± standard deviation (SD). One-way ANOVA with *post hoc* Bonferroni correction for multiple comparisons was used for group analysis (Graphpad Prism 6.0, CA, U.S.A). A non-parametric Mann-Whitney Rank Sum test was used for group comparison. The reproducibility of PAT measures of $\Delta SO_2$, quantified by using the Pearson correlation analysis of the value obtained at test and retest (n = 10). The correlation between CBF and $CMRO_2$ was analyzed using the Person correlation analysis. Significance was set at * $p < 0.05$, ** $p < 0.01$, *** $p < 0.001$.

## 3. Results

### 3.1. Sensitivity and repeatability of PAT for detecting physiological changes in blood oxygenation

Alterations in Hb and $HbO_2$ during an oxygen challenge were measured using PAT in cortical tissue, the MCA and the SSS of 12-weeks-old wild-type mice. From those measurements mean values of $\Delta SO_2$ and were calculated for each condition based on the final min within the 3-min challenge after a stable state was reached.

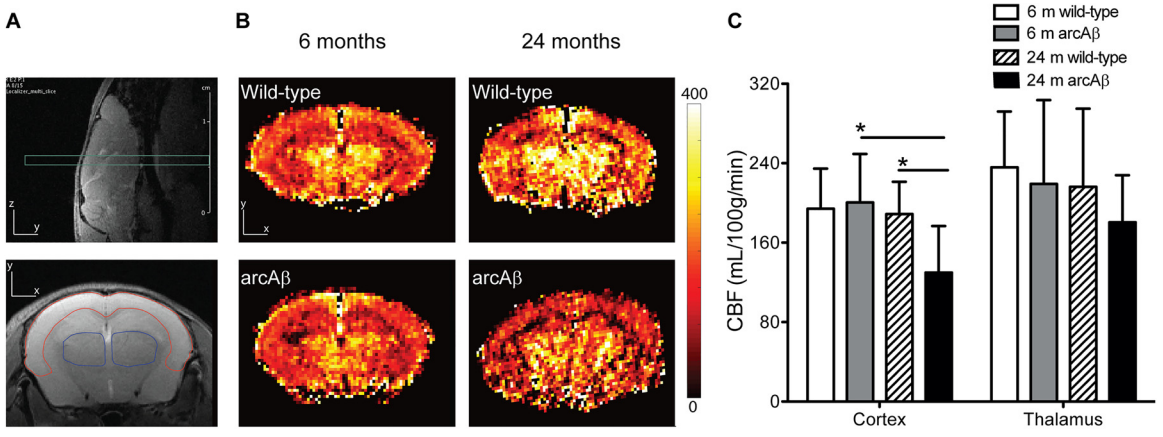


**Fig. 3.** Regional hypoperfusion in aged arcAβ mice. (A) Anatomical position of perfusion MRI and $T_2$-weighted scan on the sagittal view of the anatomical reference image and representative regions of interest (cortex (red) and thalamus (blue)) on coronal $T_2$-weighted anatomical image acquired at the same position as the ASL slice; (B) Representative coronal CBF map (approximatly Bregma −1.5 ± 0.3 mm) of 6- and 24-months-old wild-type littermate (upper row, $n = 8, 7$) and arcAβ mice (lower row, $n = 8, 8$); (C) Reduced CBF in the cortex of 24-months old arcAβ compared with age-matched wild-type mice; Reduced CBF in the cortex of arcAβ mice at 24-months compared to 6-months. *$p < 0.05$, one-way ANOVA with *post hoc* Bonferroni correction for multiple comparison; CBF, cerebral blood flow; ASL, arterial spin labeling.

The time course of delta changes, representative four coronal maps for normoxic and hyperoxic conditions are shown in the Supplementary Fig. 1. During hyperoxia higher levels of $HbO_2$ and correspondingly reduced values for Hb have been found in all compartments analyzed when compared to the normoxic reference: values for $HbO_2$ were $16.95 \pm 1.51$ *vs* $16.45 \pm 0.47$ a.u. ($p < 0.001$) for cortical tissue, $29.55 \pm 1.57$ vs $25.10 \pm 0.69$ a.u. ($p < 0.001$) for the SSS, and $7.18 \pm 0.98$ vs $6.46 \pm 0.32$ a.u. ($p < 0.001$) for the MCA; while values for Hb were $17.14 \pm 1.81$ vs $18.60 \pm 0.72$ a.u. ($p < 0.001$)) for the cortical tissue, $6.54 \pm 1.41$ vs $10.82 \pm 1.13$ a.u. ($p < 0.001$) for the SSS, and $0.01 \pm 0.01$ vs $0.14 \pm 0.05$ a.u. ($p < 0.001$) during hyperoxia vs normoxia for the MCA respectively.

Maps of $SO_2$ and a $\Delta SO_2$ were derived from PAT measurements of Hb and $HbO_2$. Fig. 1A–C shows a representative coronal $SO_2$ and a $\Delta SO_2$ map co-registered with $T_2$-weighted MRI images of a wild-type mouse during oxygen challenge. Both cortical $S_tO_2$ and $S_vO_2$ with normoxia (3–6 and 9–12 min) and hyperoxia (0–3, 6–9 and 12–15 min) revealed a robust increase in oxygenation during hyperoxia (Fig. 1C), while changes detected were smaller in $S_aO_2$ values. Hyperoxia led to a significant increase in cortical $S_tO_2$ from $47.38 \pm 0.42\%$ to $50.51 \pm 0.71\%$ ($p < 0.001$) and of SvO2 from $75.32 \pm 1.13$ % to $86.67 \pm 1.18$ % ($p < 0.001$) compared to normoxia, whereas the respective arterial value were SaO2 $99.37 \pm 0.93$ % to $99.66 \pm 0.34$ % (non-significant) (Fig. 1D,E). The OEF was calculated according to Eq. (3) for the two oxygenation states of the mouse brain. The OEF was decreased almost 50 % under hyperoxic conditions as compared to normoxia ($0.13 \pm 0.05$ vs $0.24 \pm 0.06$).

The reproducibility of the PAT estimates of $S_aO_2$ and $S_vO_2$ were analyzed by Pearson correlation of test and retest values (Supplementary Fig. 2). Robust correlation was observed between the test-retest values of the entire measurement session including 3-min hyperoxia and 3 min normoxia for mean $S_vO_2$ ($r = 0.9007$,

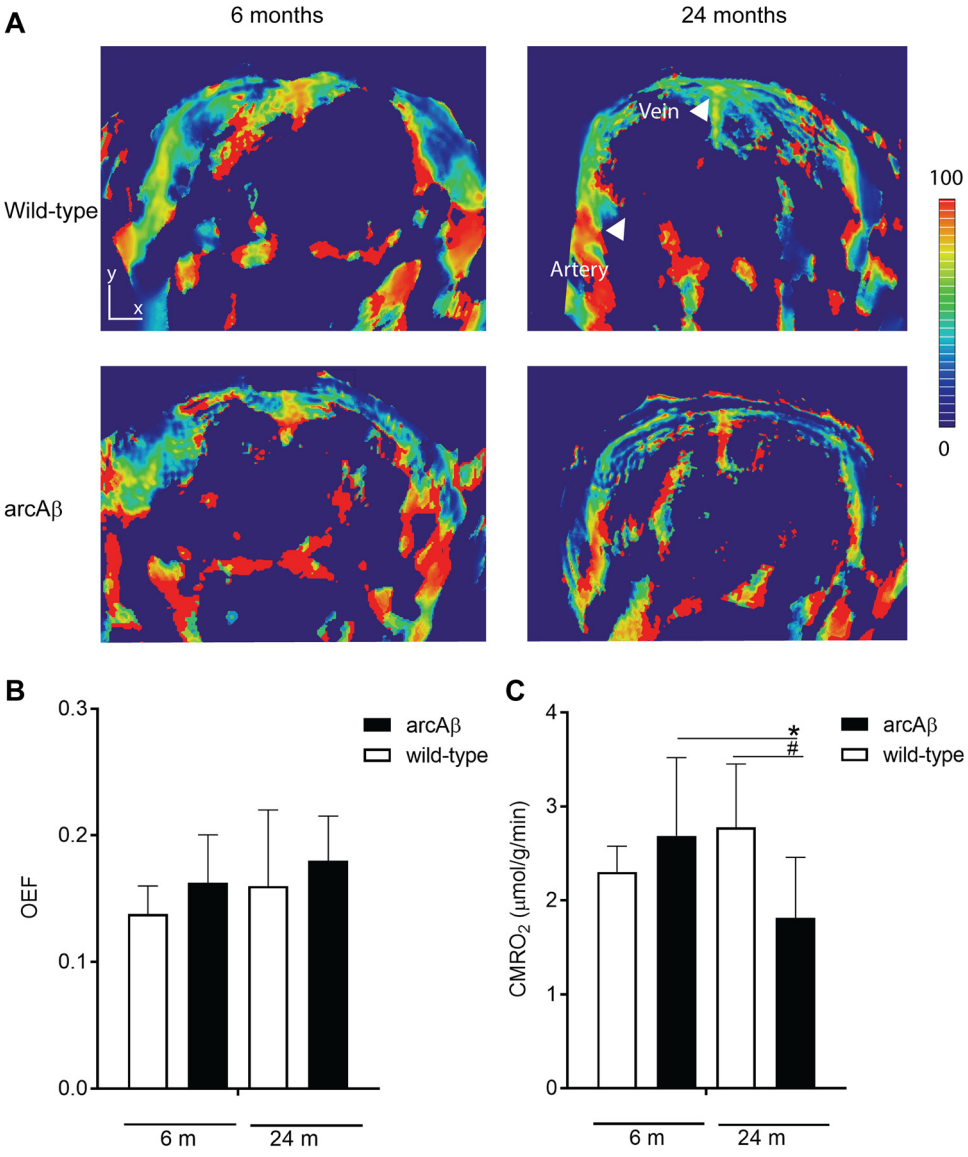


**Fig. 4.** *In vivo* assessment of brain oxygenation with PAT in arcAβ mice. (A, B) $SO_2$ maps of arcAβ and wild-type mice at 6- and 24-month (coronal view, approximately Bregma $-1.5 \pm 0.3$ mm); (b) ROIs are drawn over the middle cerebral artery (MCA) and superior sagittal sinus (SSS), scale bar = 1.5 mm images overlaid on $T_2$-weighted anatomical image; (C) Quantification of OEF and (D) $CMRO_2$ (μmol/g/min) in the brain of arcAβ and wild-type at 6-months and 24-months. $CMRO_2$ is lower in the 24-month arcAβ mouse compared to wild-type and 6-months arcAβ mice. OEF does not significantly differ in the brain of wild-type and arcAβ mice of both ages ($n = 6$-8 per group); Results are Mean ± SD, $^{*,\#}p < 0.05$, one way ANOVA with *post hoc* correction for multiple comparison; $CMRO_2$, cerebral oxygen metabolic rate; OEF, oxygenation extraction fraction; $SO_2$, oxygen saturation.

$p < 0.0001$) and mean $S_aO_2$ ($r = 0.2721$, $p = 0.0010$) of the ten wild-type mice. Correlation of the test-retest value of each mouse was also observed for $S_vO_2$ under normoxia ($r = 0.949$, $p < 0.0001$) and hyperoxia ($r = 0.8662$, $p = 0.0012$). Due to small variation in the value of $S_aO_2$ (close to 1), no correlation was observed for the test-retest comparison of each mouse.

Physiological parameters and peripheral oxygen saturation of mice were monitored on the mouse hind limb using an oximeter for 15 min under the same oxygen supply paradigm and anesthesia conditions as during the PAT measurement (Fig. 2). The peripheral $S_tO_2$ assessed by oximetry significantly increased by 0.9% under hyperoxia compared to normoxia ($97.74 \pm 0.16\%$ *vs* $96.85 \pm 0.27\%$, $p < 0.0001$). No statistically significant differences were observed in heart rate, breath distention, pulse distention and breath rate between two breathing conditions.

### 3.2. Age dependent reduction of CBF in the cortex of arcAβ mice by using perfusion MRI

CBF-MRI measurements were performed with ASL in arcAβ and wild-type mice of both 6- and 24-months of age to assess age-dependent differences in cerebral perfusion due to Aβ deposition and cerebral amyloid angiopathy. ROI analysis of CBF MRI maps showed similar levels of CBF in the cortex and thalamus between arcAβ and wild-type mice at 6-months of age (Fig. 3A–C). A 30% reduction of CBF was observed in the cortex of arcAβ mice at 24-months compared to aged-matched wild-type mice, while the levels of CBF in the thalamus were not significantly different between groups. There was no age-related effect on brain perfusion in wild-type animals: similar CBF values have been obtained for 6-months and 24-months mice both in the cortical and thalamic ROIs.

### 3.3. Reduced $CMRO_2$ values in arcAβ mice compared to wild-type littermates

We used PAT to determine the OEF and calculate $CMRO_2$ using the CBF derived from perfusion MRI in 6 months- and 24-month old arcAβ mice and the corresponding age-matched littermates under normoxic conditions ($FiO_2$ 36%). PAT covered a brain volume of 8 mm in rostral caudal direction. Fig. 4A shows the $SO_2$ in the coronal section of the brain of wild-type and arcAβ mice at 6- and 24-month of age. PAT measured OEF values derived from $S_{a/v}O_2$ did not differ between 24-months arcAβ mice ($0.18 \pm 0.04$, $n = 8$), age-matched wild-type mice ($0.16 \pm 0.06$, $n = 7$), 6-months arcAβ ($0.16 \pm 0.04$, $n = 7$) and wild-type mice ($0.14 \pm 0.02$, $n = 7$) (Fig. 4B–C). Correspondingly, the calculated $CMRO_2$ values were lower in the 24-months arcAβ mice ($1.81 \pm 0.64$ a.u., $n = 7$) compared to age-matched wild-type mice ($2.8 \pm 0.67$ a.u., $n = 5$, $p = 0.0338$) and 6-months arcAβ ($2.7 \pm 0.8$ a.u., $n = 7$, 0.0346). In contrast, the $CMRO_2$ did not differ between the 6-months arcAβ and wild-type mice ($2.30 \pm 0.27$ a.u., $n = 7$). The $CMRO_2$ correlated with CBF in arcAβ and wild-type mice (*** $p < 0.0001$, $r = 0.6987$, $n = 26$), and within arcAβ and mice (*** $p < 0.0006$, $r = 0.7975$, $n = 14$).

## 4. Discussion

PAT constitutes an attractive alternative to PET and MRI for non-invasive assessment of metrics of brain oxygenation and metabolism with whole brain coverage and high spatial resolution in mice. The technique exploits the absorption spectrum of hemoglobin, which depends on the oxygen concentration. Previous studies have used photoacoustic imaging and tomography to measure hemodynamic parameters such as CBF, cerebral blood volume, vessel diameter, total, deoxy- and oxygenated hemoglobin, and thus oxygen saturation in large vessels at resting state and during functional stimulation in the brain of mice [35–37]. In this study we identified individual large blood vessels such as the MCA which has a vessel diameter of approximately 140 μm [38] and the SSS. Our PAT system did not allow assessing oxygenation in the microvasculature, which is below the spatial resolution of 150 μm. However, photoacoustic microscopy has been used to provide hemodynamic measures down to the capillary level, though such systems have the trade-off of lower penetration depth and/or are invasive [19,20]. The PAT measures of metrics of $S_aO_2$ and $S_vO_2$ derived from measurements of Hb and $HbO_2$ of the artery and vein under normoxia of 99.37% and 75.32% found in the current study are similar to the values of 98 − 100% and 80 − 89% for arterial and venous blood respectively, as reported previously [19,39]

It should be noted that PAT does not provide absolute quantification of $SO_2$ due to several factors: First, significant light absorption in the brain and extracerebral tissue affects the incident light fluence and hence the detected signal amplitude [33]. We have shown previously that measurements of Hb and $HbO_2$ are limited to a depths of 4–5 mm [31]. Hence, for absolute quantification fluence correction and knowledge of the Grüneisen parameter [32,33] characterizing the thermoexpansion is required. Secondly, the light attenuation by tissue (or any absorber) depends on the absorption spectrum, i.e. the relative contribution of tissue depth layers to the signal will vary across the spectrum. Calibration of the attenuation may improve quantification of oxygenation [41].

The repetition of the hyperoxia-normoxia challenge demonstrated good reproducibility of the results (Supplementary Fig. 2). The high temporal resolution of (2.5 s) of the method revealed an equilibration time of 2 min upon changing the oxygen level of the inspiration gas, largely reflecting physiological adaptation. Calculation of mean $SO_2$ values at steady state showed that a hyperoxic challenge increases $S_aO_2$ by only 0.3%. This is due to the fact that arteries are already highly oxygenated under normoxic conditions. Therefore $S_aO_2$ can only modestly increase in comparison to veins where $S_vO_2$ is lower, in line with previous reports [42]. Measured increases of ~10-13% in venous $S_vO_2$ have been reported [37,39] comparable to our result of a 13% increase. The change in $S_tO_2$ was 6.5%, and reflects an averaged $S_tO_2$ value comprising arterial, venous and capillary contributions. Thus, increasing the oxygen level in the inspiration gas from 20 to 100% gave rise to only a 3.13% increase in cortical $S_tO_2$. In the periphery, the change in $S_tO_2$ was estimated to be 0.9% using a mouse oximeter. Our study, in line with previous reports demonstrates that PAT yields robust and reproducible metrics of blood and tissue oxygenation. While absolute values of Hb and $HbO_2$ may vary even under identical experimental conditions, the $SO_2$ values derived from these measurements were found to be highly reproducible (Supplementary Figs. 1 and 2).

Estimation of measures of oxygen metabolism such as OEF and $CMRO_2$ requires knowledge of CBF. Several photoacoustic methods have been proposed to measure CBF using photoacoustic microscopy [43]. However, such a method was not implementable with our current PAT system. We opted to use ASL MRI to assess cerebral perfusion as the method yields quantitative CBF values and is applicable in a straightforward manner also in humans. Co-registering of maps of Hb and $HbO_2$ with $T_2$-weighted MR images yielded an anatomical reference for ROIs delineation, where specific brain regions are more difficult to delineate. The arcAβ and littermate cohorts were measured in slightly hyperoxic (i.e. $FiO_2$ 36%) conditions due to the mixture of the breathing gas we used for anesthesia. In littermates, cortical OEF and $CMRO_2$ values of ~ 0.16 and 2.6-2.7 μmol/g/min have been derived, in accordance with values from the literature measured with $^{15}O$ PET and $^{17}O$ MR spectroscopy [44–46] and photoacoustic microscopy [19]. Aging has been reported to decrease both OEF and $CMRO_2$ in the brain of humans [47,48]. This was not observed in our study: we did not

find any statistically significant difference in measures of OEF and $CMRO_2$ in wild-type mice of 6- and 24-months of age. However, $CMRO_2$ but not OEF was found to be significantly decreased in arcAβ mice at 24-months of age. While animals at 6-months of age are devoid of parenchymal amyloid plaques, 24-months old mice display widespread parenchymal plaque deposition as well as vascular amyloid pathology [12,27]. This indicates that the reduced $CMRO_2$ in these mice is not an age-effect but is rather associated with the advanced amyloid pathology. We found that cortical CBF measured by perfusion MRI was reduced in 24-months old arcAβ mice, which under physiological conditions would result in an increase in OEF. Yet OEF values in these animals were similar to those found in wild-type mice and 6-months old arcAβ mice. This indicates that the cortical hypoperfusion observed during the advanced disease stage is not compensated by an adaptation of OEF in order to maintain $CMRO_2$ within the normal range or the metabolisms of the brain is compromised. CBF correlated with $CMRO_2$ values.

Previous studies in APP mouse models of AD have assessed cerebral perfusion but not cerebral oxygen metabolism. A reduced regional CBF was reported for strains with cerebral amyloid angiopathy deposition such as APP23, Tg2576, APP DSL, APPswe/PS1ΔE9 mice, but not in APP/PS1 mouse without cerebral amyloid angiopathy burden, indicating a strong contribution of cerebral amyloid angiopathy to the perfusion deficit [49–53]. Earlier studies from our group showed age-related vascular remodeling and significant reduced density of functional intracortical microvessels of arcAβ mice [14], which has also strong cerebral amyloid angiopathy, and impaired vascular reactivity in the cortex but not in the subcortical regions [54]. Reduced CBF and increased OEF have been reported in patients with AD [3,55], and there is an increasing awareness that vascular and metabolic alternations play an important role in the pathogenesis of AD [56]. At an early stage, a loss of cerebral perfusion pressure, which would result in decreased CBF, is compensated by an increase in cerebral blood volume. As cerebral autoregulation becomes increasingly compromised, decreasing CBF values will be counteracted by increases in OEF to maintain $CMRO_2$ in physiological range. Brain hypoperfusion and low oxygen availability can affect brain protein synthesis, lead to neuronal dysfunction [2], and an increase in APP processing, thus aggravating Aβ deposition [57]. At an advanced disease stage, this compensatory mechanism becomes exhausted leading to tissue hypoxia ischemia, which ultimately will translate into loss of neurons and tissue damage and thus a reduced $CMRO_2$. Hence, hemodynamic parameters in AD might be important read-outs for disease staging and for monitoring therapeutic interventions targeting vascular dysfunction.

There are several limitations in this study: 1) ROIs drawn for the MCA and SSS are inevitably small because of the spatial resolution of our PAT system. It is expected that a system with a higher resolution will provide a better accuracy of the signal measurements. 2) We computed OEF and $CMRO_2$ only for the cortex. The brain region is mainly supplied by the MCA and drained via cortical veins that connect to the SSS, vessels that could be easily identified on the $Hb/HbO_2$ and $SO_2$ maps. Other brain regions might be more difficult to assess e.g. the thalamus is supplied by smaller branching arteries, some of which originated from the internal carotid artery and posterior cerebral artery, which we currently cannot resolve with PAT. 3) Anesthesia affects cerebral oxygen metabolism: a recent study showed a dose-dependent decrease in OEF and $CMRO_2$ during isoflurane anesthesia in comparison to comparison to awake animals [19]. As a result, the measured values of OEF and $CMRO_2$ are likely to be higher when measured in wake mice. While this may affect the quantitative comparison of OEF and $CMRO_2$ values in wild-type and arcAβ mice, it would not affect the qualitative result, i.e. that aged arcAβ mice display reduced $CMRO_2$ values. 4) The technique is not easily translatable for human imaging. While application in some tissue such as the skin, breast [58], abdomen for Crohn's Disease [59] and tumor [60] has been demonstrated already, application to the human brain is difficult, hampered by the presence of the skull.

## 5. Conclusion

Our results show that PAT can derive metrics of $SO_2$ in single feeding and draining vessels and cortical tissue. PAT can sensitively and robustly detect physiological changes in blood oxygenation as demonstrated in oxygen challenge experiments. Furthermore, the approach can yield in conjunction with CBF derived from perfusion MRI, measures of brain oxygen metabolism. Application into transgenic arcAβ mice showed that at advanced disease stage involving cerebral amyloidosis and cerebral amyloid angiopathy cortical perfusion becomes significantly decreased. Due to the inability of the vascular system to compensate the decrease in oxygen delivery by increasing the OEF, $CMRO_2$ values were found to be significantly decreased, likely putting the tissue under hypoxic stress.

## Author contributions

RN and JK conceived and designed the study; RN performed the experiments; RN and JK analyzed the data; RN, MR and JK interpreted the results; RN and JK wrote the paper; all coauthors contributed constructively to the manuscript.

## Funding

This work was funded by the University of Zurich and the ETH Zurich Foundation through a Seed Grant of "University Medicine Zurich/Hochschulmedizin Zürich", funding from the Olga Mayenfisch Stiftung and University of Zurich Forschungskredit (Nr. FK-17-052).

## Ethical approval and consent to participate

All experiments were performed in accordance with the Swiss Federal Act on Animal Protection and were approved by the Cantonal Veterinary Office Zurich (permit number: ZH090-16). All procedures fulfill the ARRIVE guidelines on reporting animal experiments.

## Consent for publication

Not applicable.

## Conflict of interest

The authors declare that there are no conflicts of interest for COI statement.

## Availability of data and material

The datasets generated and/or analyzed during the current study and the code for registration PAT and MRI are available in the repository http://doi.org/10.6084/m9.figshare.5501605 .v1
https://codeocean.com/algorithm/910653cc-f008-4573-9b8c-92dde419528c/code.

## Acknowledgements

The authors thank Dr. Felix Schlegel, Dr. Mark Augath and Jael Xandry at Institute for Biomedical Engineering, ETH Zurich for technical support. Dr. Thomas Sardella at iThera medical for discussion.

## Appendix A. Supplementary data

Supplementary data associated with this article can be found, in the online version, at https://doi.org/10.1016/j.pacs.2018.04.001.

## References


[1] D.D. Clarke, L. Sokoloff, Circulation and Energy Metabolism of the Brain, Basic Neurochemistry, Raven Press, New York, 1989, pp. 565–590.
[2] C. Iadecola, Neurovascular regulation in the normal brain and in Alzheimer's disease, Nat. Rev. Neurosci. 5 (5) (2004) 347–360.
[3] C. Hock, K. Villringer, F. Muller-Spahn, R. Wenzel, H. Heekeren, S. Schuh-Hofer, M. Hofmann, S. Minoshima, M. Schwaiger, U. Dirnagl, A. Villringer, Decrease in parietal cerebral hemoglobin oxygenation during performance of a verbal fluency task in patients with Alzheimer's disease monitored by means of near-infrared spectroscopy (NIRS)–correlation with simultaneous rCBF-PET measurements, Brain Res. 755 (2) (1997) 293–303.
[4] Y. Iturria-Medina, R.C. Sotero, P.J. Toussaint, J.M. Mateos-Perez, A.C. Evans, Early role of vascular dysregulation on late-onset Alzheimer's disease based on multifactorial data-driven analysis, Nat. Commun. 7 (2016) 11934.
[5] H. Fukuyama, M. Ogawa, H. Yamauchi, S. Yamaguchi, J. Kimura, Y. Yonekura, J. Konishi, Altered cerebral energy metabolism in Alzheimer's disease: a PET study, J. Nucl. Med. 35 (1) (1994) 1–6.
[6] J. Klohs, M. Rudin, D.R. Shimshek, N. Beckmann, Imaging of cerebrovascular pathology in animal models of Alzheimer's disease, Front. Aging Neurosci. 6 (2014) 32.
[7] G. Poisnel, A.S. Herard, N. El Tannir El Tayara, E. Bourrin, A. Volk, F. Kober, B. Delatour, T. Delzescaux, T. Debeir, T. Rooney, J. Benavides, P. Hantraye, M. Dhenain, Increased regional cerebral glucose uptake in an APP/PS1 model of Alzheimer's disease, Neurobiol. Aging 33 (9) (2012) 1995–2005.
[8] P.C.M. van Zijl, S.M. Eleff, J.A. Ulatowski, J.M.E. Oja, A.M. Ulug, R.J. Traystman, R. A. Kauppinen, Quantitative assessment of blood flow, blood volume and blood oxygenation effects in functional magnetic resonance imaging, Nat. Med. 4 (2) (1998) 159–167.
[9] T. Temma, M. Yamazaki, J. Miyanohara, H. Shirakawa, N. Kondo, K. Koshino, S. Kaneko, H. Iida, Sequential PET estimation of cerebral oxygen metabolism with spontaneous respiration of 15O-gas in mice with bilateral common carotid artery stenosis, J. Cereb. Blood Flow Metab. (2017) (271678×17692815).
[10] T. Christen, D.S. Bolar, G. Zaharchuk, Imaging brain oxygenation with MRI using blood oxygenation approaches: methods, validation, and clinical applications, AJNR Am. J. Neuroradiol. 34 (6) (2013) 1113–1123.
[11] R.G. Wise, A.D. Harris, A.J. Stone, K. Murphy, Measurement of OEF and absolute CMRO2: MRI-based methods using interleaved and combined hypercapnia and hyperoxia, NeuroImage 83 (2013) 135–147.
[12] J. Klohs, I.W. Politano, A. Deistung, J. Grandjean, A. Drewek, M. Dominietto, R. Keist, F. Schweser, J.R. Reichenbach, R.M. Nitsch, I. Knuesel, M. Rudin, Longitudinal assessment of amyloid pathology in transgenic ArcAbeta mice using multi-Parametric magnetic resonance imaging, PLoS One 8 (6) (2013) e66097.
[13] J. Klohs, A. Deistung, G.D. Ielacqua, A. Seuwen, D. Kindler, F. Schweser, M. Vaas, A. Kipar, J.R. Reichenbach, M. Rudin, Quantitative assessment of microvasculopathy in arcAbeta mice with USPIO-enhanced gradient echo MRI, J. Cereb. Blood Flow Metab. 36 (9) (2016) 1614–1624.
[14] J. Klohs, C. Baltes, F. Princz-Kranz, D. Ratering, R.M. Nitsch, I. Knuesel, M. Rudin, Contrast-enhanced magnetic resonance microangiography reveals remodeling of the cerebral microvasculature in transgenic ArcAbeta mice, J. Neurosci. 32 (5) (2012) 1705–1713.
[15] S.P. Chong, C.W. Merkle, C. Leahy, V.J. Srinivasan, Cerebral metabolic rate of oxygen (CMRO2) assessed by combined Doppler and spectroscopic OCT, Biomed. Opt. Express 6 (10) (2015) 3941–3951.
[16] M.D. Stern, D.L. Lappe, P.D. Bowen, J.E. Chimosky, G.A. Holloway Jr., H.R. Keiser, R.L. Bowman, Continuous measurement of tissue blood flow by laser-doppler spectroscopy, Am. J. Physiol. 232 (4) (1977) H441–H448.
[17] S. Sakadzic, E. Roussakis, M.A. Yaseen, E.T. Mandeville, V.J. Srinivasan, K. Arai, S. Ruvinskaya, A. Devor, E.H. Lo, S.A. Vinogradov, D.A. Boas, Two-photon high-resolution measurement of partial pressure of oxygen in cerebral vasculature and tissue, Nat. Methods 7 (9) (2010) 755–759.
[18] B. Hallacoglu, A. Sassaroli, M. Wysocki, E. Guerrero-Berroa, M. Schnaider Beeri, V. Haroutunian, M. Shaul, I.H. Rosenberg, A.M. Troen, S. Fantini, Absolute measurement of cerebral optical coefficients, hemoglobin concentration and oxygen saturation in old and young adults with near-infrared spectroscopy, J. Biomed. Opt. 17 (8) (2012) (081406-1).
[19] R. Cao, J. Li, B. Ning, N. Sun, T. Wang, Z. Zuo, S. Hu, Functional and oxygen-metabolic photoacoustic microscopy of the awake mouse brain, NeuroImage 150 (2017) 77–87.
[20] J. Yao, L. Wang, J.M. Yang, K.I. Maslov, T.T. Wong, L. Li, C.H. Huang, J. Zou, L.V. Wang, High-speed label-free functional photoacoustic microscopy of mouse brain in action, Nat. Methods 12 (5) (2015) 407–410.
[21] L. Li, L. Zhu, C. Ma, L. Lin, J. Yao, L. Wang, K. Maslov, R. Zhang, W. Chen, J. Shi, L.V. Wang, Single-impulse panoramic photoacoustic computed tomography of small-animal whole-body dynamics at high spatiotemporal resolution, Nat. Biomed. Eng. 1 (2017) (0071).
[22] D. Razansky, C. Vinegoni, V. Ntziachristos, Multispectral photoacoustic imaging of fluorochromes in small animals, Opt. Lett. 32 (19) (2007) 2891–2893.
[23] R. Weissleder, V. Ntziachristos, Shedding light onto live molecular targets, Nat. Med. 9 (1) (2003) 123–128.
[24] M. Merlini, E.P. Meyer, A. Ulmann-Schuler, R.M. Nitsch, Vascular beta-amyloid and early astrocyte alterations impair cerebrovascular function and cerebral metabolism in transgenic arcAbeta mice, Acta Neuropathol. (Berl.) 122 (3) (2011) 293–311.
[25] A. Taruttis, V. Ntziachristos, Advances in real-time multispectral optoacoustic imaging and its applications, Nat. Photon. 9 (4) (2015) 219–227.
[26] L. Wang, K. Maslov, L.V. Wang, Single-cell label-free photoacoustic flowoxigraphy in vivo, Proc. Natl. Acad. Sci. U. S. A. 110 (15) (2013) 5759–5764.
[27] M. Knobloch, M. Farinelli, U. Konietzko, R.M. Nitsch, I.M. Mansuy, Abeta oligomer-mediated long-term potentiation impairment involves protein phosphatase 1-dependent mechanisms, J. Neurosci. 27 (29) (2007) 7648–7653.
[28] M. Vaas, R.Q. Ni, M. Rudin, A. Kipar, J. Klohs, Extracerebral tissue damage in the intraluminal filament mouse model of middle cerebral artery occlusion, Front. Neurol. 8 (2017) 85.
[29] C. Leithner, K. Gertz, H. Schrock, J. Priller, K. Prass, J. Steinbrink, A. Villringer, M. Endres, U. Lindauer, U. Dirnagl, G. Royl, A flow sensitive alternating inversion recovery (FAIR)-MRI protocol to measure hemispheric cerebral blood flow in a mouse stroke model, Exp. Neurol. 210 (1) (2008) 118–127.
[30] X. Zhang, E.T. Petersen, E. Ghariq, J.B. De Vis, A.G. Webb, W.M. Teeuwisse, J. Hendrikse, M.J. van Osch, In vivo blood T(1) measurements at 1.5 T, 3 T, and 7 T, Magn. Reson. Med. 70 (4) (2013) 1082–1086.
[31] R. Ni, M. Vaas, W. Ren, J. Klohs, Non-invasive detection of acute cerebral hypoxia and subsequent matrix-metalloproteinase activity in a mouse model of cerebral ischemia using multispectral-optoacoustic-tomography, Neurophotonics 5 (2018).
[32] D.K. Yao, C. Zhang, K. Maslov, L.V. Wang, Photoacoustic measurement of the Gruneisen parameter of tissue, J. Biomed. Opt. 19 (1) (2014) 17007.
[33] M.R. Tomaszewski, I.Q. Gonzalez, J.P. O'Connor, O. Abeyakoon, G.J. Parker, K.J. Williams, F.J. Gilbert, S.E. Bohndiek, Oxygen enhanced optoacoustic tomography (OE-OT) reveals vascular dynamics in murine models of prostate cancer, Theranostics 7 (11) (2017) 2900–2913.
[34] F. Xu, Y. Ge, H. Lu, Noninvasive quantification of whole-brain cerebral metabolic rate of oxygen (CMRO2) by MRI, Magn. Reson. Med. 62 (1) (2009) 141–148.
[35] M.L. Li, J.T. Oh, X.Y. Xie, G. Ku, W. Wang, C. Li, G. Lungu, G. Stoica, L.V. Wang, Simultaneous molecular and hypoxia imaging of brain tumors in vivo using spectroscopic photoacoustic tomography, Proc. IEEE 96 (3) (2008) 481–489.
[36] J. Yao, J. Xia, K.I. Maslov, M. Nasiriavanaki, V. Tsytsarev, A.V. Demchenko, L.V. Wang, Noninvasive photoacoustic computed tomography of mouse brain metabolism in vivo, NeuroImage 64 (2013) 257–266.
[37] S. Gottschalk, T.F. Fehm, X.L. Dean-Ben, D. Razansky, Noninvasive real-time visualization of multiple cerebral hemodynamic parameters in whole mouse brains using five-dimensional optoacoustic tomography, J. Cereb. Blood Flow Metab. 35 (4) (2015) 531–535.
[38] K. Kidoguchi, M. Tamaki, T. Mizobe, J. Koyama, T. Kondoh, E. Kohmura, T. Sakurai, K. Yokono, K. Umetani, In vivo X-ray angiography in the mouse brain using synchrotron radiation, Stroke 37 (7) (2006) 1856–1861.
[39] X. Wang, X. Xie, G. Ku, L.V. Wang, G. Stoica, Noninvasive imaging of hemoglobin concentration and oxygenation in the rat brain using high-resolution photoacoustic tomography, J. Biomed. Opt. 11 (2) (2006) 024015.
[41] S. Tzoumas, A. Nunes, I. Olefir, S. Stangl, P. Symvoulidis, S. Glasl, C. Bayer, G. Multhoff, V. Ntziachristos, Eigenspectra optoacoustic tomography achieves quantitative blood oxygenation imaging deep in tissues, Nat. Commun. 7 (2016) 12121.
[42] S. Sakadzic, E.T. Mandeville, L. Gagnon, J.J. Musacchia, M.A. Yaseen, M.A. Yucel, J. Lefebvre, F. Lesage, A.M. Dale, K. Eikermann-Haerter, C. Ayata, V.J. Srinivasan, E.H. Lo, A. Devor, D.A. Boas, Large arteriolar component of oxygen delivery implies a safe margin of oxygen supply to cerebral tissue, Nat. Commun. 5 (2014) 5734.
[43] P.J. van den Berg, K. Daoudi, W. Steenbergen, Review of photoacoustic flow imaging: its current state and its promises, Photoacoustics 3 (3) (2015) 89–99.
[44] T. Temma, Y. Kuge, K. Sano, J. Kamihashi, N. Obokata, H. Kawashima, Y. Magata, H. Saji, PET O-15 cerebral blood flow and metabolism after acute stroke in spontaneously hypertensive rats, Brain Res. 1212 (2008) 18–24.
[45] W. Cui, X.H. Zhu, M.L. Vollmers, E.T. Colonna, G. Adriany, B. Tramm, J.M. Dubinsky, G. Oz, Non-invasive measurement of cerebral oxygen metabolism in the mouse brain by ultra-high field (17)O MR spectroscopy, J. Cereb. Blood Flow Metab. 33 (12) (2013) 1846–1849.
[46] X.H. Zhu, J.M. Chen, T.W. Tu, W. Chen, S.K. Song, Simultaneous and noninvasive imaging of cerebral oxygen metabolic rate, blood flow and oxygen extraction fraction in stroke mice, NeuroImage 64 (2013) 437–447.
[47] H. Takada, K. Nagata, Y. Hirata, Y. Satoh, Y. Watahiki, J. Sugawara, E. Yokoyama, Y. Kondoh, F. Shishido, A. Inugami, et al., Age-related decline of cerebral oxygen metabolism in normal population detected with positron emission tomography, Neurol. Res. 14 (2 Suppl) (1992) 128–131.
[48] J.B. De Vis, J. Hendrikse, A. Bhogal, A. Adams, L.J. Kappelle, E.T. Petersen, Age-related changes in brain hemodynamics; A calibrated MRI study, Hum. Brain Mapp. 36 (10) (2015) 3973–3987.
[49] A. Delekate, M. Fuchtemeier, T. Schumacher, C. Ulbrich, M. Foddis, G.C. Petzold, Metabotropic P2Y1 receptor signalling mediates astrocytic hyperactivity in vivo in an Alzheimer's disease mouse model, Nat. Commun. 5 (2014) 5422.
[50] F.C. Maier, H.F. Wehrl, A.M. Schmid, J.G. Mannheim, S. Wiehr, C. Lerdkrai, C. Calaminus, A. Stahlschmidt, L. Ye, M. Burnet, D. Stiller, O. Sabri, G. Reischl, M.

Staufenbiel, O. Garaschuk, M. Jucker, B.J. Pichler, Longitudinal PET-MRI reveals beta-amyloid deposition and rCBF dynamics and connects vascular amyloidosis to quantitative loss of perfusion, Nat. Med. 20 (12) (2014) 1485–1492.
[51] H.K. Shin, P.B. Jones, M. Garcia-Alloza, L. Borrelli, S.M. Greenberg, B.J. Bacskai, M.P. Frosch, B.T. Hyman, M.A. Moskowitz, C. Ayata, Age-dependent cerebrovascular dysfunction in a transgenic mouse model of cerebral amyloid angiopathy, Brain 130 (Pt. 9) (2007) 2310–2319.
[52] B.H. Han, M.L. Zhou, F. Abousaleh, R.P. Brendza, H.H. Dietrich, J. Koenigsknecht-Talboo, J.R. Cirrito, E. Milner, D.M. Holtzman, G.J. Zipfel, Cerebrovascular dysfunction in amyloid precursor protein transgenic mice: contribution of soluble and insoluble amyloid-beta peptide, partial restoration via gamma-secretase inhibition, J. Neurosci. 28 (50) (2008) 13542–13550.
[53] H. Li, Q. Guo, T. Inoue, V.A. Polito, K. Tabuchi, R.E. Hammer, R.G. Pautler, G.E. Taffet, H. Zheng, Vascular and parenchymal amyloid pathology in an Alzheimer disease knock-in mouse model: interplay with cerebral blood flow, Mol. Neurodegener. 9 (2014) 28.
[54] F.L. Princz-Kranz, T. Mueggler, M. Knobloch, R.M. Nitsch, M. Rudin, Vascular response to acetazolamide decreases as a function of age in the arcA beta mouse model of cerebral amyloidosis, Neurobiol. Dis. 40 (1) (2010) 284–292.
[55] S.F. Eskildsen, L. Gyldensted, K. Nagenthiraja, R.B. Nielsen, M.B. Hansen, R.B. Dalby, J. Frandsen, A. Rodell, C. Gyldensted, S.N. Jespersen, T.E. Lund, K. Mouridsen, H. Braendgaard, L. Ostergaard, Increased cortical capillary transit time heterogeneity in Alzheimer's disease: a DSC-MRI perfusion study, Neurobiol. Aging 50 (2017) 107–118.
[56] K. Nagata, Y. Kondoh, R. Atchison, M. Sato, Y. Satoh, Y. Watahiki, Y. Hirata, E. Yokoyama, Vascular and metabolic reserve in Alzheimer's disease, Neurobiol. Aging 21 (2) (2000) 301–307.
[57] X. Sun, G. He, H. Qing, W. Zhou, F. Dobie, F. Cai, M. Staufenbiel, L.E. Huang, W. Song, Hypoxia facilitates Alzheimer's disease pathogenesis by up-regulating BACE1 gene expression, Proc. Natl. Acad. Sci. U. S. A. 103 (49) (2006) 18727–18732.
[58] S. Manohar, S.E. Vaartjes, J.C. van Hespen, J.M. Klaase, F.M. van den Engh, W. Steenbergen, T.G. van Leeuwen, Initial results of in vivo non-invasive cancer imaging in the human breast using near-infrared photoacoustics, Opt. Express 15 (19) (2007) 12277–12285.
[59] F. Knieling, C. Neufert, A. Hartmann, J. Claussen, A. Urich, C. Egger, M. Vetter, S. Fischer, L. Pfeifer, A. Hagel, C. Kielisch, R.S. Gortz, D. Wildner, M. Engel, J. Rother, W. Uter, J. Siebler, R. Atreya, W. Rascher, D. Strobel, M.F. Neurath, M.J. Waldner, Multispectral optoacoustic tomography for assessment of crohn's disease activity, N. Engl. J. Med. 376 (13) (2017) 1292–1294.
[60] I. Stoffels, S. Morscher, I. Helfrich, U. Hillen, J. Leyh, N.C. Burton, T.C.P. Sardella, J. Claussen, T.D. Poeppel, H.S. Bachmann, A. Roesch, K. Griewank, D. Schadendorf, M. Gunzer, J. Klode, Metastatic status of sentinel lymph nodes in melanoma determined noninvasively with multispectral optoacoustic imaging, Sci. Transl. Med. 7 (317) (2015) (317ra199-317ra199).

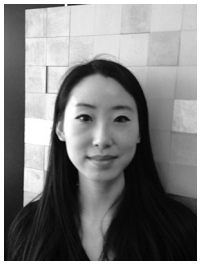

**Dr. Ruiqing Ni** obtained her BSc in Pharmacy at the Fudan University, Shanghai, China. She completed a Ph.D. in Medicine (Neuroscience programme) at the Karolinska Institutet, Stockholm, Sweden, and a short-term JSPS fellowship postdoc at National Institute of Radiological Science Japan. She is currently a postdoctoral research at ETH Zurich/University of Zurich. Her research focuses on the development of positron emission tomography, optical imaging and magnetic resonance imaging biomarkers for early diagnosis of Alzheimer's disease.

**Prof. Markus Rudin** obtained Ph.D. at the Laboratory for Physical Chemistry at ETH Zurich in the field of electron spin resonance/electron-nuclear double resonance, followed by a post-doctorate in the same area. He is a full professor for Molecular Imaging and Functional Pharmacology at the Institute for Biomedical Engineering at ETH Zurich and University of Zürich. His research focus is the development of non-invasive imaging techniques for studying structure, physiology, and metabolism of tissue as well as cellular and molecular events in the intact organism, in particular assays for monitoring signal transduction pathways.

**Prof. Jan Klohs** obtained a BSc degree in Chemistry at the University of Wales, Swansea, United Kingdom. He completed a MSc and Ph.D. in Medical Neurosciences at the Charité –University Medicine Berlin, Germany. He is currently an assistant professor for preclinical imaging at the University of Zurich. His research focuses on the development of optical imaging and magnetic resonance imaging techniques, and investigations of preclinical models of brain disease.